Received: 10 October 2024 | Revised: 3 August 2025 | Accepted: 20 August 2025

DOI: 10.1002/mp.18090

RESEARCH ARTICLE

MEDICAL PHYSICS

Transcranial ultrasound tomography for brain imaging: Ex vivo results and potential for stroke imaging

Trevor Mitcham[1] | **Rehman Ali**[1] | **Melanie Singh**[2] | **Sarah McConnell**[3] | **Redi Rahmani**[4] | **Derrek Schartz**[1] | **Matthew Bender**[5] | **Edward Vates**[5] | **Neb Duric**[1,2]

[1]Department of Imaging Sciences, University of Rochester, Rochester, New York, USA

[2]Department of Biomedical Engineering University of Rochester, Rochester, New York, USA

[3]Department of Neuroscience, University of Rochester, Rochester, New York, USA

[4]Department of Neurosurgery, University of Louisville, Louisville, Kentucky, USA

[5]Department of Neurosurgery, University of Rochester, Rochester, New York, USA

Correspondence
Trevor Mitcham, Department of Imaging Sciences, University of Rochester Medical Center, 601 Elmwood Ave, Rochester, NY 14642, USA.
Email: Trevor_Mitcham@URMC.Rochester.edu

Abstract

Background: Stroke is a leading cause of death and disability in America and around the world. Due to the differences in underlying cause and clinical treatment between ischemic and hemorrhagic stroke, it is critical to perform imaging before administration of treatment. The current clinical standard is to image patients with computed tomography or magnetic resonance imaging, which creates a major delay in stroke treatment because paramedics have to transport patients to a major medical center before imaging can even begin. Therefore, there is an unmet need to provide imaging at the point of injury for stroke patients, so that therapeutic intervention can occur faster.

Purpose: This work investigates the feasibility of using ultrasound tomography (UST) with full waveform inversion (FWI) image reconstruction as a point-of-injury tool to help provide faster stroke triage, using in silico, in vitro, and ex vivo imaging phantoms

Methods: In silico image data were simulated for three datasets, which each include skull, brain, and a unique hemorrhage. These data were reconstructed with two different frequency ranges; one (100–700 kHz) to simulate an ideal hardware setup, and the other (300–700 kHz) to represent the limitations of our current image acquisition system. Next, a replica skull was filled with a brain-mimicking gelatin phantom and three regions of blood to simulate hemorrhage prior to imaging and reconstruction to visualize the blood contrast in a realistic environment. Then, a preserved macaque brain was imaged both outside of and within the replica skull to demonstrate our ability to visualize anatomical landmarks and the effects generated by the skull. Finally, an intact human cadaveric brain was imaged to demonstrate our ability to resolve important anatomical landmarks in a relevant model.

Results: In silico experiments show that UST is capable of imaging anatomical landmarks and hemorrhage pathologies through the skull, despite artifacts when starting FWI reconstruction at 300 kHz. The in vitro hemorrhage phantom also demonstrated that hemorrhages as small as 0.7 cm in diameter can be visualized through the replica skull using UST. Multiple features, such as the interhemispheric fissure, sylvian fissures, ventricles, and the brain stem could be visualized in the macaque brain when imaged in a water bath, and these features remained visible even when the brain was placed within the replica skull despite additional artifacts. Finally, the human brain was visualized with UST, showing high-resolution images with significant anatomical detail. Ultimately, the images presented in this work demonstrate the level of detail which can

ultimately be achieved using this technique in the absence of the skull, which will guide future development.

Conclusion: This work shows that UST imaging of the brain is feasible through a skull-mimicking phantom for a variety of targets. In silico, in vitro and ex vivo targets could all be visualized in sound speed images with a skull phantom present despite the presence of cycle skipping artifacts. Additionally, an intact human brain sample was imaged to demonstrate our current ability to visualize anatomical features, and therefore guide future development of this work.

KEYWORDS
neuroimaging, transcranial, ultrasound tomography

1 | INTRODUCTION

Per the American Heart Association, stroke is the fifth leading cause of death in the United States and the leading cause of disability.[1] Approximately 140,000 Americans die from strokes every year, while the annual costs to the healthcare system exceed $50 billion. Stroke is a colloquial term, which includes both interruption of blood flow (i.e., ischemic stroke) and bleeding within the brain (i.e., hemorrhagic stroke).[1,2] While both types of stroke can lead to severe brain damage, ultimately these two categories require vastly different treatment approaches.[3] Hemorrhagic stroke is treated with hemostatic drugs to reduce potential hematoma expansion within the first 24–48 h after injury and/or open surgical clot evacuation via a craniotomy.[4–6] Ischemic stroke, on the other hand, is treated in part with clot-dissolving medications or percutaneous mechanical thrombectomy, but the presence of concurrent bleeding must first be ruled out on imaging. However, delays in treatment have a direct impact on the recovery process and the level of disability experienced post-treatment.[7] To this end, timely treatment is important because the typical stroke patient loses 1.9 million neurons each minute ischemic stroke goes untreated; therefore, "time is brain".[8]

In order to differentiate between the two types of strokes in a timely manner, imaging is a key step for triaging and stroke treatment planning. Standard clinical workflow includes using computed tomography (CT) or magnetic resonance imaging to rule out hemorrhage, both of which require transporting the patient to a nearby hospital.[2] In practice, the time needed to transport the patient to a hospital and acquire imaging are major factors that influence stroke outcomes (i.e., the time needed for therapeutic intervention).[3] Imaging for triage is currently a significant barrier and presents an opportunity for modalities that can be deployed *before and during* patient transport to the hospital. Therefore, some hospitals use mobile CT ambulances or Mobile Stroke Units.[9] However, these options are not widely available, especially in rural and under-resourced areas owing to high capital and maintenance expenses.[10] As a result, point-of-injury brain imaging for rapid stroke assessment and triaging is a major unmet need in many areas. Ideally, a portable, low-cost device that can be carried in a typical ambulance and used at the site (e.g., the patient's home), would make early interventions widely available thereby minimizing delays in treatment and positively impacting stroke recovery.[11]

One potential candidate to address this goal is ultrasound tomography (UST) imaging. UST has emerged as a clinical modality capable of quantitatively imaging in vivo tissue parameters with high resolution using the transmission of ultrasound through tissue. The main clinical use of UST is breast cancer screening in dense breast tissue as an adjunct to mammography, although the FDA also provided clearance for diagnostic breast imaging use. Currently, the most common application of UST uses sound speed, attenuation, and reflection images in combination to detect breast tumors in patients with dense breast tissue which are hard to diagnose with mammography alone.[12–16] Unlike conventional pulse-echo ultrasound modalities, UST images provide absolute estimates of sound speed, density, and acoustic attenuation through full-waveform inversion (FWI) reconstruction algorithms, while also utilizing the reflected signals to generate 360-degree reflection images which can inherently be corrected for sound speed aberrations. Current clinical ring-array-based UST uses a frequency-domain FWI algorithm to generate diagnostic-quality images in a clinically relevant reconstruction timeframe.[17] Furthermore, multimodal UST imaging is being investigated to provide additional benefits for breast cancer detection; mammography and UST fusion images can be generated to provide improved co-registration,[18] while photoacoustic imaging can be combined with UST to provide functional information about the chromophores present within the area of interest.[19,20] These investigations demonstrate the potential for extended applications of UST beyond adjunct breast cancer screening.

In addition to work on breast imaging, ultrasound imaging of the brain through the skull has become a topic of increased interest in recent years.[21] While countless papers have been published on conventional

B-Mode reflection imaging of the brain, these studies are generally limited to the acoustic windows within the skull and are not able to map the sound speed, attenuation, and density of the tissue in the same way that UST images can. The first UST images of the head were successfully acquired and reconstructed in the 1970s, using ray-based image reconstructions to visualize donor human head samples, but these acquisitions provided images with low spatial resolution and poor soft tissue contrast within the skull.[22,23] Since then, many studies have been published using in silico models to demonstrate the potential of this application with novel reconstruction methods, although many of these have not been experimentally validated.[24–27] Additionally, several studies have investigated phantom and animal data acquisition, demonstrating that UST imaging through bone is possible.[28–32] However, at this time, there has not been an image generated of a physical ex vivo primate or human brain using UST with FWI reconstruction methods. Therefore, in this work, we investigate the feasibility of using UST with FWI image reconstruction to characterize various hemorrhages using simulation data and in vitro phantoms. Furthermore, we investigate the ability to visualize normal brain anatomy, through the skull, with ex vivo animal data. Finally, we image a preserved human brain to assess the visibility of normal human brain anatomy to use as a reference for future human studies.

2 | METHODS

2.1 | K-wave simulation images

Initial in silico experiments utilized the MATLAB k-wave toolbox to simulate ultrasonic propagation through three brain hemorrhage models.[33] A normal head CT scan[34] was used to derive the model via the piecewise fitting of Hounsfield Units to density and sound speed,[35] and an intercranial hemorrhage (ICH), subarachnoid hemorrhage (SAH), or subdural hematoma (SDH) inclusion is added to reflect the acoustic properties of whole blood based on literature values.[36] The ultrasound imaging simulation models a broadband low frequency ring transducer (1024 elements, 22 cm diameter). To produce the RF data, the simulated transducer emits a single cycle Gaussian pulse with a center frequency of 1 MHz. The pulse maintains a 75% fractional bandwidth at the −6 dB reference level.

Reconstructed sound speed images are achieved through our existing FWI algorithms,[37,38] described below, and the reconstructed images were then compared to the "truth" images (Figure 1a), to benchmark ideal UST image quality and define limitations. For FWI reconstruction, the initial model utilized a homogeneous medium modeled as water (1500 m/s sound speed). Then, two different FWI reconstructions were preformed using distinct frequency ranges. The first reconstruction mirrored the frequency content available in our current hardware system and utilized frequency values from 300 to 700 kHz with 50 kHz steps. The second reconstruction, which utilizes the frequency content that would come from an ideal acquisition system, used frequency values from 50 to 700 kHz with 5 kHz steps.

2.2 | Image acquisition, reconstruction, and analysis

For all physical experiments, single-slice UST imaging was performed on a Verasonics Vantage 256 system (Verasonics Inc., Kirkland, WA) with a 1024-element ring array (Figure 2; Transducer Works, LLC, Centre Hall, PA; 3 MHz center frequency, 1–4 MHz Bandwidth),[39] using a Verasonics UTA 1024 MUX adaptor to allow for multiplexing between transducer elements. In all image sequences, data were acquired by firing one element at a time, with all individual elements receiving the signal, until the full dataset is collected. No sub-apertures were used. Unless stated otherwise, the transducer was driven at 700 kHz to ensure appropriate low frequency content in the waveform to begin FWI image reconstruction.[38]

Reconstruction was then performed using frequency-domain FWI techniques (350–700 kHz, 50 kHz step size, 1540 m/s homogeneous starting model) to generate sound speed images, while traditional reflection images were also generated to aid with localization of the features. To briefly describe the FWI algorithm, the 2D Helmholtz equation is used to simulate the ultrasound signal that would be recorded by the ring array for a given sound speed profile in the medium. The result of the simulation is then compared to measured data at the ring array at discrete frequencies, starting at the lowest available frequency (e.g., 350 kHz) and subsequently bootstrapping up to the highest required frequency (e.g., 700 kHz) with set spacing (e.g., every 50 kHz).[37] By iteratively backprojecting the error between the simulated and measured signal at each frequency, FWI reconstructs the sound speed profile that minimizes this error. This reconstruction sequence allows FWI to first establish the coarse low-frequency spatial details, and then subsequently fill in the fine, high-frequency spatial details at the subsequent higher imaging frequencies to provide the final image. The final FWI-based sound speed map is then used by the traditional delay-and-sum reflection algorithm to correct for sound-speed-induced aberrations. Therefore, instead of an assumption of a constant sound speed throughout the medium, the sound speed image is used to provide a heterogeneous sound speed map which is used to reduce sound-speed-based aberration within the delay-and-sum image.

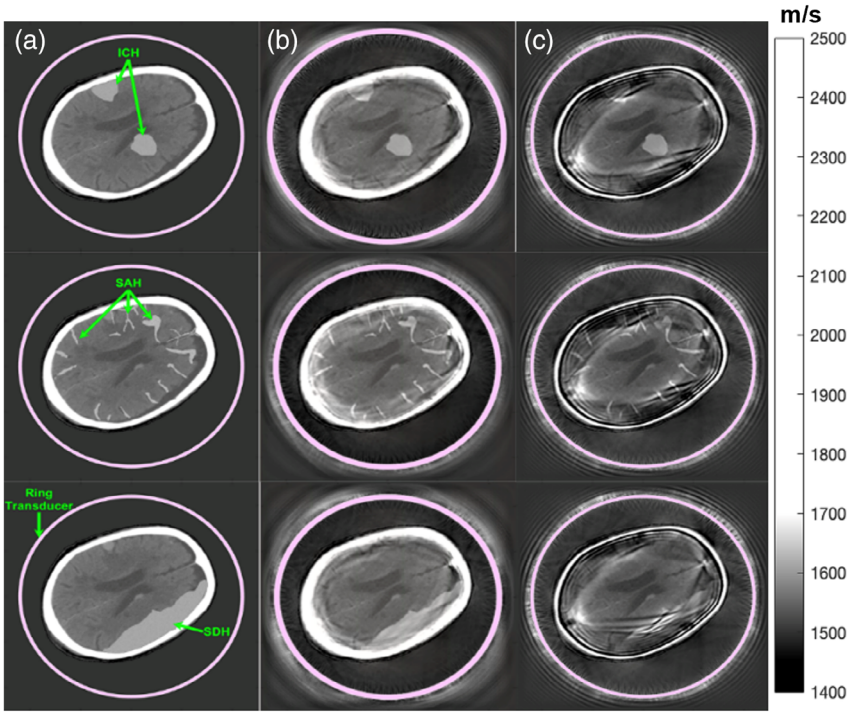

FIGURE 1 Numerical models and their sound speed reconstructions. (a) SAH, SDH, and ICH ground truth models. (b) FWI reconstructions using $f = 50–700$ KHz. (c) Reconstructions using $f = 300–700$ kHz, mimicking the limitations of our experimental setup.

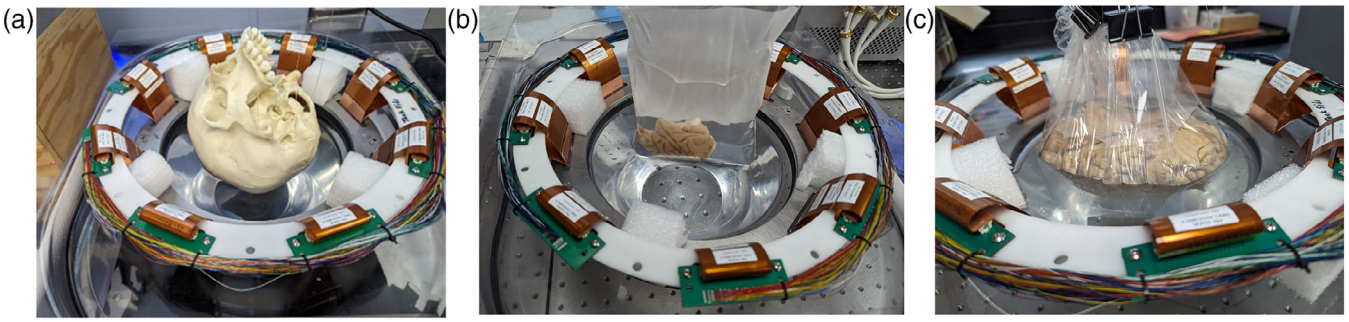

FIGURE 2 Visualization of imaging setup (including 1024-element ring array transducer) for: (a) In vitro phantoms using the skull-mimicking phantom, (b) ex vivo macaque brain, and (c) ex vivo human brain inside a plastic bag for support and isolation from the surrounding water bath.

For all experiments, quantitative analysis was performed on sound speed images generated from the FWI reconstruction as previously stated. Unless stated otherwise, three independent circular ROIs (5-mm diameter) were placed over each identified image feature to calculate the mean sound speed values which were reconstructed in the images. Values are reported as the mean across all three ROIs with the standard deviation across the three ROIs as the error. Additionally, each ROI was expanded to create an annulus of equal area completely surrounding the original ROI with the same centroid. Information from both the original circular ROI and the secondary annulus ROI were used to calculate SNR and CNR as follows:

$$SNR = \frac{S_i}{\sigma_o} \tag{1}$$

$$CNR = \frac{S_i - S_o}{\sqrt{\sigma_i^2 + \sigma_o^2}} \tag{2}$$

where S_i is the mean signal inside the circular ROI, S_o is the mean signal inside the surrounding annulus, σ_i is the standard deviation within the circular ROI, and σ_o is the standard deviation inside the surrounding annulus.

2.3 | Skull-mimicking phantom characterization

After validating that in silico experiments can provide diagnostic image quality, a human replica skull (Skulls Unlimited Inc., Oklahoma City, OK) was used to demonstrate our current ability to image through bone-mimicking material (Figure 2a). Using the ring

array transducer and an Onda HNA 0400 hydrophone (Onda Corporation, Sunnyvale, CA), amplitude and travel time measurements were collected in a water bath (21°C) with and without the skull phantom to measure the changes in sound speed and attenuation of the material prior to further experiments.

2.4 | In vitro hemorrhage imaging

Next, the same skull-mimicking phantom was utilized to image a simulated cerebral hemorrhage. The skull phantom was first filled with a mixture of 8% gelatin (Sigma-Aldrich, Inc., St. Louis, MO) and 0.5% silica powder (US Silica, Katy, TX). Three cylindrical molds were cast within the gelatin to provide wells that could be used to simulate bleeding. One large well with a slightly irregular border (3 cm diameter) and two small wells (0.8 cm diameter) were injected with whole ex vivo human blood from the University of Rochester Vascular Tissue bank (IRB # 6999), and subsequently imaged with UST using the previously stated imaging parameters described in section 2.2. As the smaller hemorrhage inclusions were too small to allow for multiple ROIs, one ROI was placed in each of the three inclusions and averaged together for quantitative analysis.

2.5 | Ex vivo imaging of intact macaque brain

The next experiment utilized an intact macaque brain which had been preserved in a 10% formalin solution. The brain was rehydrated in 10 mM PBS (pH 7.4) for two weeks prior to imaging to reduce tissue stiffness, and then imaged in two different scenarios. First, the sample was placed inside a transparent plastic bag filled with 10 mM PBS solution, and then imaged at multiple elevational slices to characterize the acoustic properties and anatomical landmarks throughout the full volume, providing a baseline image quality for brain tissue (Figure 2b). Images were then repeated with the preserved brain sample within the skull-mimicking phantom to show the effects of the skull phantom on the ability to image anatomical features.

2.6 | Ex vivo imaging of intact human brain

Finally, in order to demonstrate our ultimate ability to resolve anatomical features in a human brain, we imaged an intact donor brain specimen (provided through the anatomical gift program at the University of Rochester School of Medicine and Dentistry) which had been embalmed using a formaldehyde solution and subsequently preserved in a solution of 50% ethanol and 50% water. To facilitate UST imaging while maintaining the integrity of the sample, it was placed inside a plastic bag filled with distilled water and then imaged at multiple elevational slices to characterize the acoustic properties throughout the full volume (Figure 2C).

Images of the brain were reconstructed using a novel method referred to as frequency differencing FWI (FD-FWI) to overcome artifacts generated by the artificially high sound speed resulting from the tissue preservation process. In short, this method utilizes existing US signal to generate new low-frequency content, providing an improved starting model to begin FWI reconstruction. To facilitate this reconstruction method, data were acquired by driving the transducer at 2.5 MHz (i.e., near the transducer's central frequency). Frequency content from 1.0 to 5.0 MHz is used to generate signal between 0.05 and 1.0 MHz with 50 kHz spacing. The FWI algorithm then iterates through each of these low-frequency signals twice to generate the new starting model, which is then introduced to the standard FWI algorithm previously described in Section 2.2.[40] Sound speed analysis was performed as in Section 2.2, with all ROIs within common tissue types grouped together for analysis.

3 | RESULTS

3.1 | In silico imaging

K-Wave simulations support our hypothesis that UST is capable of imaging pathologies through the skull, providing a roadmap for experimental work (Figure 1). Artifacts due to cycle skipping and high sound speed contrast are minimized when beginning reconstruction at 50 kHz, while anatomical features of the brain as well as intercranial hemorrhage (Figure 1a), subarachnoid hemorrhages (Figure 1b), and subdural hematomas (Figure 1c) can be visualized clearly within the simulated imaging datasets.

3.2 | Skull-mimicking phantom characterization

The skull phantom was shown to have a sound speed of approximately 2450 m/s, and an attenuation of 5.5 dB/cm when using a 1 MHz transmission from the ring array transducer. While the attenuation value is lower than expected in the skull of a live patient, the sound speed closely mimics that of human bone.[41]

3.3 | In vitro hemorrhage imaging

Despite the presence of artifacts, all three hemorrhages could be visualized within the skull-mimicking phantom

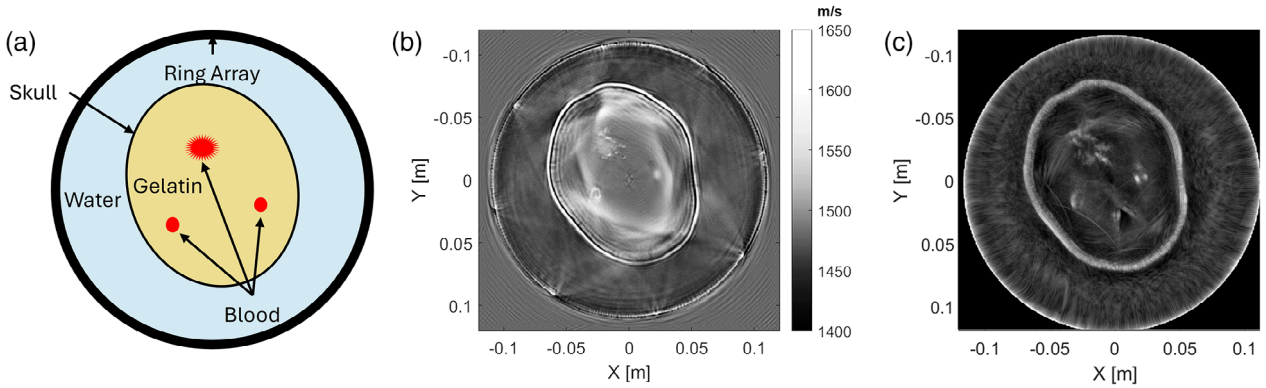

FIGURE 3 (a) Annotated diagram of the in vitro hemorrhage phantom with three ex vivo blood inclusions in (b) FWI-based sound speed, and (c) reflection images. Both images clearly show the three inclusions despite artifacts.

in sound speed and reflection images (Figure 3). The background gelatin medium showed an average sound speed value of 1521 ± 9 m/s, while hemorrhages showed an average sound speed of 1564 ± 5 m/s. The border of the large inclusion shows irregularities where gelatin was removed when the phantom mold was removed from the background. Cycle skipping artifacts in Figure 3b appear as a bright ring through the center of the phantom, while reverberation artifacts can be seen in the reflection image in Figure 3c. The mean CNR across the three inclusions was 0.65 ± 0.05, while the mean SNR was 42.3 ± 1.9 dB.

3.4 | Ex vivo macaque brain characterization

Multiple anatomic features, including the interhemispheric fissure, Sylvian fissure, ventricles, and the brain stem, can be visualized in sound speed and reflection images (Figure 4).[42,43] Overall, sound speed values within the preserved brain ranged from 1500 to 1580 m/s, which is approximately consistent with the increased stiffness expected in preserved tissue.[44,45]

Without the skull phantom, sound speed values for the Interhemispheric Fissure, Sylvian Fissures, and ventricles were measured at 1508 ± 5, 1502 ± 6, and 1507 ± 2 m/s, respectively, all of which are consistent with PBS at 21°C.[46] Additionally, the average sound speed of brain tissue across all image slices was 1543 ± 4 m/s without the skull phantom present. In reflection images, the same features can be resolved, with the interfaces of the interhemispheric fissure, Sylvian fissures, and ventricles showing as hyper-echoic within the images.

With the skull phantom present, the brain sample could still be resolved in both reconstructions, and the Sylvian and interhemispheric fissures can be clearly visualized (Figure 4d). Sound speed values of anatomical features show minimal changes when compared to the original baseline values, with the interhemispheric fissure, Sylvian fissures, and brain tissue showing sound speed values of 1505 ± 5 m/s, 1503 ± 8 m/s, and 1537 ± 8 m/s, respectively. ROIs averaged throughout the macaque brain showed a mean SNR of 43.7 ± 1.9 dB.

3.5 | Human donor brain

Sound speed and reflection images were reconstructed in both sagittal and axial imaging planes within the preserved human brain sample. Within the sagittal image slice (Figure 5a), multiple anatomical features can be visualized including the cerebral cortex, white/gray matter boundary, corpus callosum, lateral ventricle, 4th ventricle, quadrigeminal cistern, cerebellum, pons, and medulla. In the inferior axial view (Figure 5b), the corpus callosum, lateral ventricles, choroid plexus, thalamus, quadrigeminal cistern, and cerebellum can be visualized, while the superior axial slice clearly shows the interhemispheric fissure, cerebral cortex, and the boundary between white and grey matter. While some artifacts remain in the images, they are correlated across both image reconstructions and generally do not detract from our ability to visualize anatomic features.

Within the sound speed images, regions of fluid accumulation (i.e., lateral and 4th ventricles, quadrigeminal cistern, and the interhemispheric fissure) could easily be distinguished from brain tissue. Sound speed within the lateral ventricle was measured to be 1670 ± 2 m/s, demonstrating isolation of the alcohol mixture within the deep cavity (Figure 5a,b). Meanwhile, the sound speed in the 4th ventricle was measured to be 1615 ± 4 m/s, and 1582 ± 3 m/s in the quadrigeminal cistern, showing that the distilled water had mixed with the preservative fluid in these cavities (Figure 5a,b). Within regions of brain tissue, structures composed of white matter appear different than structures composed of gray matter in sound speed images, with 1639 ± 3 m/s for

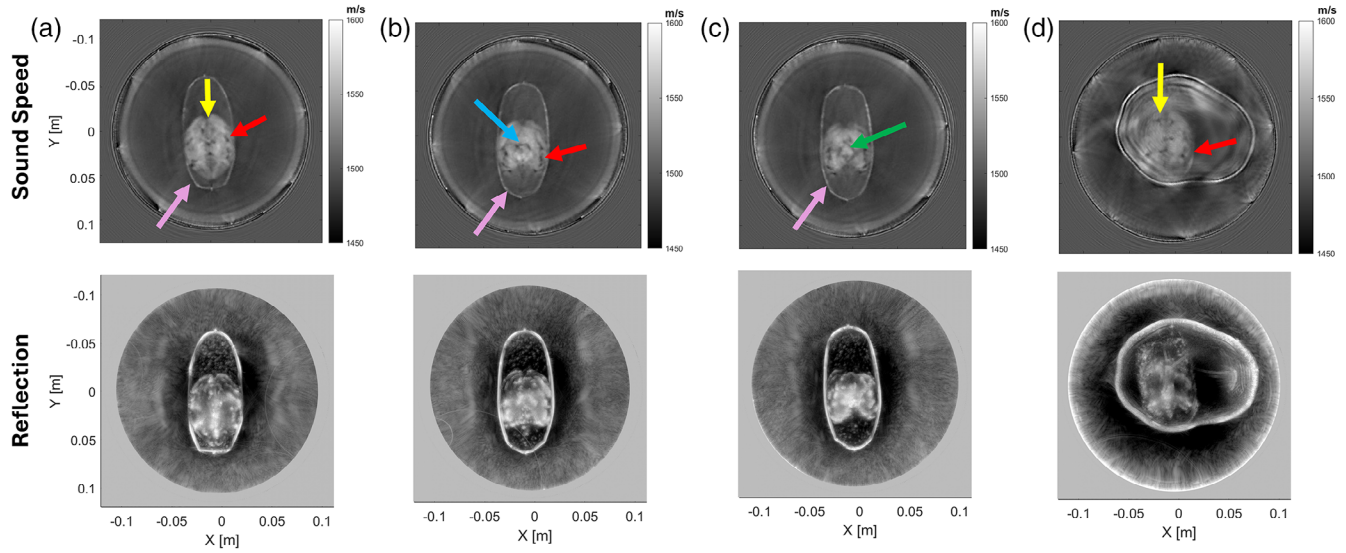

FIGURE 4 Macaque brain images. Sound speed images in the top row are paired with a matching reflection image on the bottom row. Purple arrows show the plastic bag used for the brain sample. (a) Axial cross-section showing the interhemispheric fissure (yellow) and sylvian fissures (red). (b) Axial cross-section showing the ventricles (blue) and sylvian fissures (red). (c) Axial cross-section showing the brain stem (green). (d) Axial cross-section within the skull-mimicking phantom showing the interhemispheric fissure (yellow) and sylvian fissures (red).

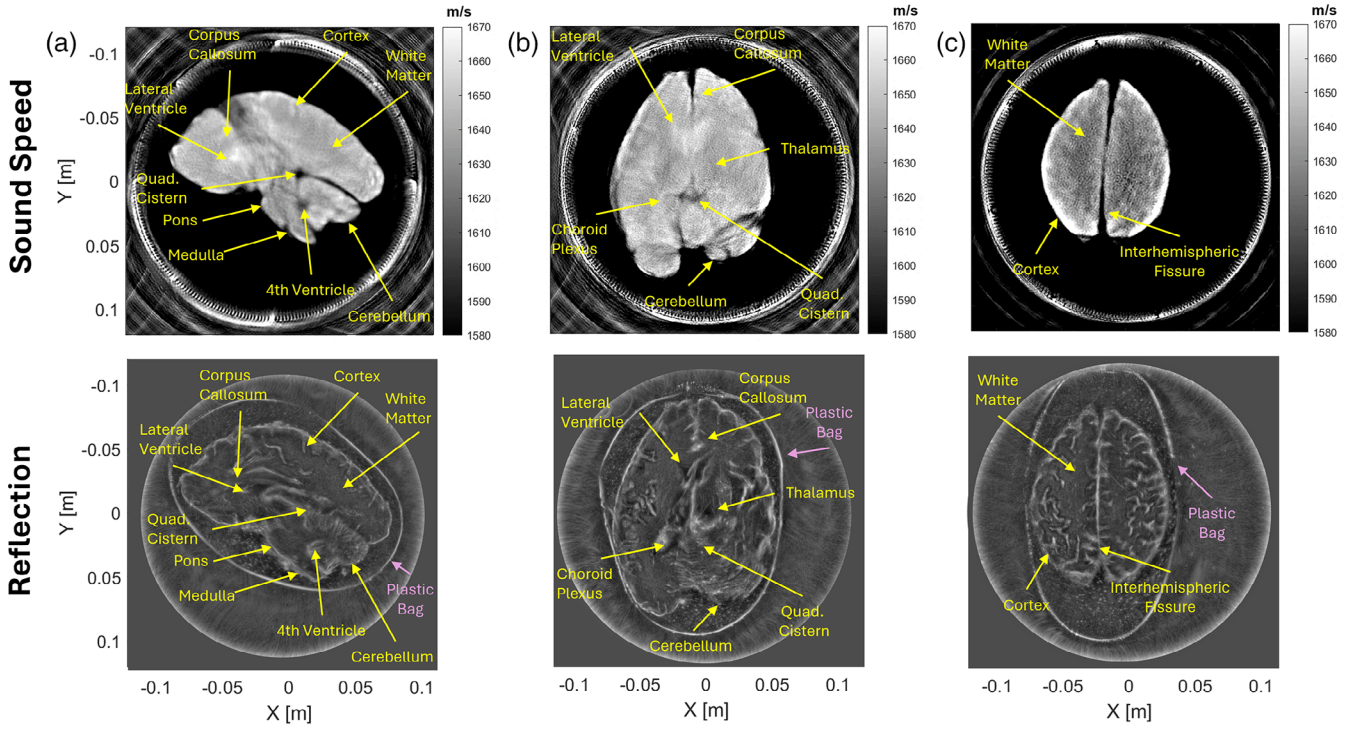

FIGURE 5 Donor human brain images showing sound speed (top) and reflection (bottom) reconstructions. (a) Sagittal view showing the cerebral cortex, white/gray matter boundary, corpus callosum, lateral ventricle, 4th ventricle, quadrigeminal cistern, cerebellum, pons, and medulla. (b) Inferior axial view showing the corpus callosum, lateral ventricles, choroid plexus, thalamus, quadrigeminal cistern, and cerebellum. (c) Superior axial view showing the interhemispheric fissure, cerebral cortex, and the boundary between white and grey matter.

white matter and 1656 ± 6 m/s for gray matter. Features such as the corpus callosum and region inferior to the cortex (i.e., white matter) display slower sound speed than structures comprised of gray matter, such as the cerebellum, thyroid, choroid plexus, and cortex (Figure 5a–c). Finally, structures with mixed composition such as the pons and medulla show heterogeneous sound speed in the images (Figure 5a). SNR remained

consistent across all tissue types, with a mean SNR of 43.0 ± 3.6 dB when averaged across all samples.

Within reflection images, additional detail can be resolved to supplement the quantitative sound speed maps. While the sound speed maps show minimal variation between the structures comprised of gray matter, they provide quantitative information. Conversely, the reflection images provide structural boundaries to help visualize each individual anatomical feature but lack quantitation.

4 | DISCUSSION

In this work, we present validation that UST imaging can detect multiple hemorrhage types in a realistic simulation environment, while also detecting ex vivo whole blood within a tissue-mimicking phantom environment in real experimental data. Additionally, we characterize our ability to visualize the anatomy of a macaque brain both with and without a skull-mimicking material, as well as our ability to visualize the anatomy of a standalone ex vivo human brain sample to demonstrate the ultimate potential of this technique. These results show that UST imaging is feasible through a skull-mimicking phantom, although further work is needed to optimize both the image acquisition and reconstruction due to the presence of artifacts.

When analyzing UST images, it is important to consider the unique information provided by different reconstruction methods. Reflection images, much like traditional B-Mode images, can provide clear anatomical detail, as tissue boundaries show up due to the acoustic impedance mismatch. However, these images provide limited quantitative information, as is typical from reflection US images. On the other hand, the sound speed images are able to clearly show quantitative differences in tissue composition across the brain, and in blood samples. These quantitative sound speed maps allow for quantitative verification of tissue type within the brain (e.g., white vs. grey matter), but have less clear boundaries for anatomical details. The ultimate goal of this work is to generate a system capable of using both image types to localize irregular anatomical features with reflection images while using sound speed imaging to analyze the composition of the feature (e.g., hemorrhage).

Simulation images show the ultimate potential of this work, providing a roadmap for what could be accomplished with a specialized transcranial UST acquisition system. Reconstructed images starting at 300 kHz show cycle skipping artifacts. Additionally, errors are noted when reconstructing the skull-brain interface, where, for example, the reconstructed skull appears smaller than it should be, while a region of low sound speed fills the space between the inner skull boundary and the brain. This is likely due to the high difference in sound speed between the skull and the surrounding soft tissue, causing the FWI algorithm to converge to an incorrect solution. When lowering the starting frequency of the reconstruction, while also limiting the step size of the reconstruction algorithm, these artifacts are minimized, providing improved visualization of the anatomy of interest within the skull. Therefore, dedicated acquisition hardware which allows for imaging at or below 100 kHz should help improve image quality of transcranial UST images by unlocking optimal FWI reconstruction techniques.

In the first experiment using physical data, ex vivo whole blood was visualized very clearly across both reconstructions with minimal artifacts present, even in the presence of the skull phantom (Figure 3). The cycle skipping and refraction artifacts present in the images can likely be attributed to limitations in the FWI reconstruction process, owing in part to unavailability of sufficiently low frequency data as previously discussed. While present, these artifacts do not impede our ability to visualize all three blood inclusions within the brain-mimicking background in the sound speed image. As the data acquisition system was originally designed for breast cancer screening, as is typical for current UST systems, we currently lack high SNR data below 300 kHz to mitigate these artifacts with the current hardware setup.

In addition to the in vitro phantom experiment, the ex vivo macaque brain provides insight into the ultimate goal of this work. Across all elevational slices, multiple anatomic features can be clearly visualized in both reconstructions, demonstrating that UST imaging can provide sufficient detail of normal brain anatomy, even though the skull. Multiple key anatomic landmarks are visible within the images, such as the interhemispheric fissure, Sylvian fissure, ventricles, and the brain stem. In the future, abnormalities in each of these features, such as displacement from excessive blood or changes in the material properties of the fluid filling the space, could be utilized to diagnose hemorrhage via imaging.[47] While artifacts degrade overall image quality when the brain is within the skull-mimicking phantom, diagnostically important features (e.g., interhemispheric fissure) can still be distinguished. As is mirrored in the simulation study, the areas nearest the skull phantom demonstrate the greatest image degradation, while the region near the center of the skull cavity are reconstructed relatively cleanly. Therefore, this result demonstrates the importance of further modifying our imaging acquisition and reconstruction methods so that we can better visualize the whole brain, including the areas near the skull.

The final experiment presented in this work was to designed to image the whole brain (without a skull) in order to demonstrate high resolution UST imaging and to develop an atlas of anatomical features to use as a reference in future human studies where the brain

would be imaged through the skull. To the best of our knowledge, the three visualizations of the intact human brain in Figure 5 represent the first high-resolution UST images of an intact human brain reconstructed with FWI techniques to be presented in the literature.

Reconstructed sound speeds are significantly higher than would be expected in vivo, likely due to prolonged ethanol fixation of the sample prior to imaging.[45] The storage of the intact brain specimen in 50% ethanol solution likely led to sufficient absorption in tissue to induce a net increase in overall sound speed. Conversely, the brain is not immersed in the distilled water long enough to cause major diffusion out of the alcohol-saturated tissue prior to imaging, leading to overall high sound speed values. However, it is important to note that some cavities within the brain (e.g., lateral ventricles) demonstrate significantly higher sound speed than others (e.g., 4th ventricle) due to different levels of fluid retention, leading to an alcohol-water-protein mixture within some cavities during imaging. Ultimately, this increased overall sound speed caused some issues during reconstruction with traditional waveform inversion techniques. Therefore, it was necessary to utilize our recently developed frequency-differencing waveform inversion algorithm[40] to generate an appropriate starting model, which allows for proper convergence of the algorithm throughout the sample. The average sound speed of the tissue is on the order of 1620 m/s, significantly higher than the background water sound speed (~1470 m/s), which caused significant cycle skipping artifacts in the image when using a traditional homogeneous starting model. While minor irregularities persist in the images from Figure 5a and b, they are mirrored across not only sound speed, but also reflection images which do not utilize FWI-based reconstruction techniques, demonstrating that these features may have an anatomical foundation rather than purely artifactual. Ultimately, the images presented in this work demonstrate the level of detail which can ultimately be achieved using this technique once the challenges of imaging through the skull are resolved.

The artifacts present in this work pose a particular challenge, as they can negatively impact the overall image quality enough to obscure important anatomical features. However, they can generally be overcome by addressing two sets of issues that can be loosely grouped into hardware and software concerns. Hardware concerns that must be addressed include low signal to noise ratio (SNR) at our desired imaging frequencies (i.e., 100–600 kHz levels), and a complete lack of signal at sub-300 kHz levels, leading to cycle skipping artifacts when starting FWI at these (relatively) high starting frequencies.[38] Starting FWI reconstruction at significantly lower frequencies can help to overcome cycle skipping artifacts in imaging samples with high sound speed discontinuities as we expect to see with the skull, as shown in Figure 1. Software (i.e., algorithmic) concerns include investigation of adaptive waveform inversion[48] and the introduction of an accurate image-derived two-component model[49] in order to help generate additional low frequency content and provide an accurate starting mode, respectively. Future work will focus on investigating all of these factors, via development of a transcranial-focused UST acquisition system which can provide ideal raw RF data for FWI reconstruction, and subsequent algorithm development for said data.

Finally, while the skull phantom used in these experiments does not provide fully tissue-mimicking attenuation values, the sound speed is close to that which we would expect from in vivo skull material, which provides us with a roadmap towards eliminating the cycle skipping artifacts based on sound speed discontinuities. As stated previously, we plan to develop a specialized data acquisition system optimized for brain imaging through the human skull, at which point we will also address translation to real human bone phantoms, which will present with additional attenuation as well as air pockets such as sinus cavities. We will overcome the attenuation issue via increased transmit power, virtual source transmission, and/or transmission encoding schemes to increase SNR.[50] Ultimately, to address air pockets in the skull, it may be necessary to transition to a conformable 3D transducer geometry that can be created with these problems in mind.

5 | CONCLUSIONS

This work shows that UST imaging is feasible through a skull-mimicking phantom for a variety of targets. Simulations of realistic hemorrhages, as well as in vitro and ex vivo targets could all be visualized in sound speed images despite the presence of cycle skipping artifacts. Additionally, an intact human brain sample was imaged to demonstrate our current ability to visualize anatomical features to guide future development of this work.

ACKNOWLEDGMENTS

We would like to acknowledge clinical insight provided by Dr. Deborah Rubens, we would like to thank Dr. Madalina Tivarus and Brenna Harris for providing skull CT datasets for our use, and we would also like to thank Drs. Allan Johnson, Yi Qi, and Stephanie Blocker from Duke University for providing the preserved Macaque brain sample for imaging. Finally, we would like to acknowledge funding from NIH R01 EB028652 and URMC Fischer Fund GF450257 in support of this work.

CONFLICT OF INTEREST STATEMENT

The authors have no conflicts of interest to declare.

REFERENCES

1. Heart disease and stroke statistics—2023 update: a report from the american heart association. Circulation. 2023. https://www.ahajournals.org/doi/full/10.1161/CIR.0000000000001123
2. Provost C, Soudant M, Legrand L, et al. Magnetic resonance imaging or computed tomography before treatment in acute ischemic stroke. *Stroke*. 2019;50(3):659-664. doi:10.1161/STROKEAHA.118.023882
3. Mendez B, Requena M, Aires A, et al. Direct transfer to angio-suite to reduce workflow times and increase favorable clinical outcome. *Stroke*. 2018;49(11):2723-2727. doi:10.1161/STROKEAHA.118.021989
4. Fletcher-Sandersjöö A, Tatter C, Tjerkaski J, et al. Time course and clinical significance of hematoma expansion in moderate-to-severe traumatic brain injury: an observational cohort study. *Neurocrit Care*. 2023;38(1):60-70. doi:10.1007/s12028-022-01609-w
5. Brouwers HB, Greenberg SM. Hematoma expansion following acute intracerebral hemorrhage. *Cerebrovasc Dis*. 2013;35(3):195-201. doi:10.1159/000346599
6. Gao B, Xue T, Rong X, et al. Tranexamic acid inhibits hematoma expansion in intracerebral hemorrhage and traumatic brain injury. does blood pressure play a potential role? A meta-analysis from randmized controlled trials. *J Stroke Cerebrovasc Dis*. 2021;30(1):105436. doi:10.1016/j.jstrokecerebrovasdis.2020.105436
7. Emberson J, Lees KR, Lyden P, et al. Effect of treatment delay, age, and stroke severity on the effects of intravenous thrombolysis with alteplase for acute ischaemic stroke: a meta-analysis of individual patient data from randomised trials. *Lancet*. 2014;384(9958):1929-1935. doi:10.1016/S0140-6736(14)60584-5
8. Saver JL. Time is brain—quantified. *Stroke*. 2006;37(1):263-266. doi:10.1161/01.STR.0000196957.55928.ab
9. Walter S, Kostopoulos P, Haass A, et al. Diagnosis and treatment of patients with stroke in a mobile stroke unit versus in hospital: a randomised controlled trial. *Lancet Neurol*. 2012;11(5):397-404. doi:10.1016/S1474-4422(12)70057-1
10. Fassbender K, Merzou F, Lesmeister M, et al. Impact of mobile stroke units. *J Neurol Neurosurg Psychiatry* 2021;92(8):815-822. doi:10.1136/jnnp-2020-324005
11. Mitcham T, Ali R, Schartz D, Singh M, Bender M, Duric N, Feasibility of imaging ischemic stroke through the skull using ultrasound tomography. In: *2023 IEEE International Ultrasonics Symposium (IUS)*. 2023:1-3. doi:10.1109/IUS51837.2023.10308116
12. Detection of breast cancer with ultrasound tomography: first results with the computed ultrasound risk evaluation (CURE) prototype—duric-2007. *Medical Physics*—Wiley Online Library. 2023. https://aapm.onlinelibrary.wiley.com/doi/full/10.1118/1.2432161
13. André M, Wiskin J, Borup D. Clinical results with ultrasound computed tomography of the breast. In: Mamou J, Oelze ML, eds. *Quantitative Ultrasound in Soft Tissues*. Springer Netherlands; 2013:395-432. doi:10.1007/978-94-007-6952-6_15
14. Duric N, Littrup P, Li C, et al. Breast ultrasound tomography: bridging the gap to clinical practice. In: *Medical Imaging 2012: Ultrasonic Imaging, Tomography, and Therapy*. Vol 8320. SPIE; 2012:205-213. doi:10.1117/12.910988
15. Wiskin J, Malik B, Klock J. Low frequency 3D transmission ultrasound tomography: technical details and clinical implications. *Z Für Med Phys*. 2023;33(3):427-443. doi:10.1016/j.zemedi.2023.04.006
16. O'Flynn EAM, Fromageau J, Ledger AE, et al. Ultrasound tomography evaluation of breast density. *Invest Radiol*. 2017;52(6):343-348. doi:10.1097/RLI.0000000000000347
17. Sandhu GY, West E, Li C, Roy O, Duric N, 3D frequency-domain ultrasound waveform tomography breast imaging. In: *Medical Imaging 2017: Ultrasonic Imaging and Tomography*. Vol 10139. SPIE; 2017:56-69. doi:10.1117/12.2254399
18. Hopp T, Duric N, Ruiter NV. Image fusion of ultrasound computer tomography volumes with X-ray mammograms using a biomechanical model based 2D/3D registration. *Comput Med Imaging Graph Off J Comput Med Imaging Soc*. 2015;40:170-181. doi:10.1016/j.compmedimag.2014.10.005
19. Alshahrani SS, Yan Y, Alijabbari N, et al. All-reflective ring illumination system for photoacoustic tomography. *J Biomed Opt*. 2019;24(4):1-7. doi:10.1117/1.JBO.24.4.046004
20. Goh Y, Balasundaram G, Tan HM, et al. Biochemical "decoding" of breast ultrasound images with optoacoustic tomography fusion: first-in-human display of lipid and collagen signals on breast ultrasound. *Photoacoustics*. 2022;27:100377. doi:10.1016/j.pacs.2022.100377
21. Riis TS, Webb TD, Kubanek J. Acoustic properties across the human skull. *Ultrasonics*. 2022;119:106591. doi:10.1016/j.ultras.2021.106591
22. Dines KA, Fry FJ, Patrick JT, Gilmor RL. Computerized ultrasound tomography of the human head: experimental results. *Ultrason Imaging*. 1981;3(4):342-351. doi:10.1016/0161-7346(81)90175-9
23. Carson PL, Oughton TV, Hendee WR, Ahuja AS. Imaging soft tissue through bone with ultrasound transmission tomography by reconstruction. *Med Phys*. 1977;4(4):302-309.
24. Guasch L, Calderón Agudo O, Tang MX, Nachev P, Warner M. Full-waveform inversion imaging of the human brain. *Npj Digit Med*. 2020;3(1):1-12. doi:10.1038/s41746-020-0240-8
25. Tong J, Wang X, Ren J, et al. Transcranial ultrasound imaging with decomposition descent learning-based full waveform inversion. *IEEE Trans Ultrason Ferroelectr Freq Control*. 2022;69(12):3297-3307. doi:10.1109/TUFFC.2022.3217512
26. Vassilevski YV, Beklemysheva KA, Grigoriev GK, et al. Transcranial ultrasound of cerebral vessels in silico: proof of concept. *Russ J Numer Anal Math Model*. 2016;31(5):317-328. doi:10.1515/rnam-2016-0030
27. Bouchoux G, Shivashankar R, Abruzzo TA, Holland CK. In silico study of low-frequency transcranial ultrasound fields in acute ischemic stroke patients. *Ultrasound Med Biol*. 2014;40(6):1154-1166. doi:10.1016/j.ultrasmedbio.2013.12.025
28. Soleimani M, Rymarczyk T, Kłosowski G. Ultrasound brain tomography: comparison of deep learning and deterministic methods. *IEEE Trans Instrum Meas*. 2024;73:1-12. doi:10.1109/TIM.2023.3330229
29. Cudeiro-Blanco J, Cueto C, Bates O, et al. Design and construction of a low-frequency ultrasound acquisition device for 2-D brain imaging using full-waveform inversion. *Ultrasound Med Biol*. 2022;48(10):1995-2008. doi:10.1016/j.ultrasmedbio.2022.05.023
30. Robins TC, Cueto C, Cudeiro J, et al. Dual-probe transcranial full-waveform inversion: a brain phantom feasibility study. *Ultrasound Med Biol*. 2023;49(10):2302-2315. doi:10.1016/j.ultrasmedbio.2023.06.001
31. Chen WT, Shih CC, Huang CC, High frequency ultrasound computed tomography for small animal imaging applications. In: *2011 IEEE International Ultrasonics Symposium*. 2011:1415-1418. doi:10.1109/ULTSYM.2011.0350
32. Wiskin J, Malik B, Ruoff C, Pirshafiey N, Lenox M, Klock J. Whole-body imaging using low frequency transmission ultrasound. *Acad Radiol*. 2023;30(11):2674-2685. doi:10.1016/j.acra.2023.01.018
33. k-Wave: MATLAB toolbox for the simulation and reconstruction of photoacoustic wave fields. Accessed August 20, 2023. https://www.spiedigitallibrary.org/journals/journal-of-biomedical-optics/volume-15/issue-2/021314/k-Wave–MATLAB-toolbox-for-the-simulation-and-reconstruction/10.1117/1.3360308.full

34. Hssayeni M, Computed tomography images for intracranial hemorrhage detection and segmentation. doi:10.13026/4NAE-ZG36
35. Webb TD, Leung SA, Rosenberg J, et al. Measurements of the relationship between ct hounsfield units and acoustic velocity and how it changes with photon energy and reconstruction method. *IEEE Trans Ultrason Ferroelectr Freq Control*. 2018;65(7):1111-1124. doi:10.1109/TUFFC.2018.2827899
36. Mast TD. Empirical relationships between acoustic parameters in human soft tissues. *Acoust Res Lett Online*. 2000;1(2):37-42. doi:10.1121/1.1336896
37. Ali R, Mitcham TM, Brevett T, et al. 2-D slicewise waveform inversion of sound speed and acoustic attenuation for ring array ultrasound tomography based on a block LU solver. *IEEE Trans Med Imaging*. 2024;43(8):2988-3000. doi:10.1109/TMI.2024.3383816
38. Ali R, Mitcham T, Duric N. Impact of starting model on waveform inversion in ultrasound tomography;12470:89-98. doi:10.1117/12.2653575. SPIE.
39. Acoustic tomography: Promise versus reality. IEEE Conference Publication | IEEE Xplore. 2023. https://ieeexplore.ieee.org/abstract/document/6293747/
40. Ali R, Mitcham T, Duric N. A new strategy to overcome cycle skipping: frequency-difference waveform inversion. 2024;12932:85-92. doi:10.1117/12.3006287. SPIE.
41. Pichardo S, Sin VW, Hynynen K. Multi-frequency characterization of the speed of sound and attenuation coefficient for longitudinal transmission of freshly excised human skulls. *Phys Med Biol*. 2010;56(1):219. doi:10.1088/0031-9155/56/1/014
42. Rushmore RJ, Bouix S, Kubicki M, et al. MRI-based parcellation and morphometry of the individual rhesus monkey brain: the macaque Harvard-Oxford atlas (mHOA), a translational system referencing a standardized ontology. *Brain Imaging Behav*. 2021;15(3):1589-1621. doi:10.1007/s11682-020-00357-9
43. Calabrese E, Badea A, Coe CL, et al. A diffusion tensor MRI atlas of the postmortem rhesus macaque brain. *NeuroImage*. 2015;117:408-416. doi:10.1016/j.neuroimage.2015.05.072
44. Kremkau FW, Barnes RW, McGraw CP. Ultrasonic attenuation and propagation speed in normal human brain. *J Acoust Soc Am*. 1981;70(1):29-38. doi:10.1121/1.386578
45. Tamura K, Ito K, Yoshida S, Mamou J, Miura K, Yamamoto S. Alteration of speed-of-sound by fixatives and tissue processing methods in scanning acoustic microscopy. *Front Phys. 2023*. 2024;11. Accessed. https://www.frontiersin.org/articles/10.3389/fphy.2023.1060296
46. Nehring GI, Bingham EE, Hoffmeister B, Viano A. Speed of sound of ultrasonic pulses in fluids relevant to biomedical research. *J Acoust Soc Am*. 2023;154(4):A318. doi:10.1121/10.0023657
47. Gil-Garcia CA, Flores-Alvarez E, Cebrian-Garcia R, et al. Essential topics about the imaging diagnosis and treatment of hemorrhagic stroke: a comprehensive review of the 2022 AHA guidelines. *Curr Probl Cardiol*. 2022;47(11):101328. doi:10.1016/j.cpcardiol.2022.101328
48. Adaptive waveform inversion: Theory | GEOPHYSICS. 2023. https://library.seg.org/doi/full/10.1190/geo2015-0387.1
49. Marty P, Boehm C, Fichtner A, Shape optimization for transcranial ultrasound computed tomography. 2023 | Marty | Publications | Spie. In: *SPIE Medical Imaging* 2023. Vol 12470. 77-88. Accessed August 20, 2023. https://spie.org/Publications/Proceedings/Paper/10.1117/12.2654328?SSO=1
50. Bae MH, Jeong MK. A study of synthetic-aperture imaging with virtual source elements in B-mode ultrasound imaging systems. *IEEE Trans Ultrason Ferroelectr Freq Control*. 2000;47(6):1510-1519. doi:10.1109/58.883540

How to cite this article: Mitcham T, Ali R, Singh M, et al. Transcranial ultrasound tomography for brain imaging: Ex vivo results and potential for stroke imaging. *Med Phys*. 2025;52:e18090. https://doi.org/10.1002/mp.18090